



# **Formation of a multi-translational reactivated ancient landslide in the Three Gorges Reservoir, China**

Shilin Luo<sup>1,2</sup>, Xiaoguang Jin<sup>1</sup>, Da Huang<sup>3\*</sup>, and Tantan Zhu<sup>1,3</sup>

<sup>1</sup>State Key Laboratory of Coal Mine Disaster Dynamics and Control, Chongqing University, Chongqing 400044, China

<sup>2</sup>Provincial Key Laboratory of Safe Mining Techniques of Coal Mines, Hunan University of Science and Technology, Xiangtan, Hunan, 411100, China

<sup>3</sup>School of civil and transportation engineering, Hebei University of Technology, Tianjin 300401, China

\* Corresponding author: [dahuang@hebut.edu.cn](mailto:dahuang@hebut.edu.cn)

## **Abstract**

The fluctuation of water levels and seasonal rainfall in a reservoir may induce various types of slope movements. Some of these movements are new, whereas others are old but reactivated. The primary aim of this study is to investigate the formation mechanism and process, deposit characteristics, and identification signs of a giant multi-translational reactivated ancient landslide in the Three Gorges Reservoir region based on field observations, on-site surveys, and Electron Spin Resonance experiments. The Outang landslide, located at the south bank of the Yangtze River, has a total volume of approximately 90 million m<sup>3</sup> and can be divided into three independent subzones with an apparent age of 120–130 ka (ka represents a thousand years) for subzone O1, 65–68 ka for subzone O2, and 47–49 ka for subzone O3. The features of mobilized material structure and slip surface morphology in each subzone are similar and are in the form of a spoon. A conceptual model, including sliding, bending, suspending, and accumulating, is deduced to explain the formation mechanism and evolutionary process of this instability. Three types of evidences are proposed to recognize the ancient landslide. Currently, landslide stability is obscure based on the significant landslide movement and reactivated features; more attention and long-term monitoring is necessary in the future.

**Keywords:** Three Gorges Reservoir; Ancient landslide; Formation mechanism; Evolutionary process; Recognition evidences



30

## 31 **Introduction**

32 The landslide, defined as a wide variety of processes that result in the downward and outward  
33 movements of slope-forming materials (Varnes, 1978), is a typical and destructive geo-hazard (Liu  
34 et al., 2016; Huang and Zhu 2017; Sättele et al., 2017; Jacobs et al., 2018). Typically, slope  
35 instability can be classified into the occurrence of new landslides and the reactivation of ancient  
36 landslides, both of which are extremely prevalent in reservoir areas and may create landslide dams,  
37 bury residential houses, and pose a significant threat to the natural environment (Gutiérrez et al.,  
38 2015; Gu and Huang, 2016; Huang et al., 2018). A well-known reservoir slope instability event is  
39 the 1963 Vajont landslide in Italy, where more than 2,000 deaths were reported and several villages  
40 were destroyed. Since then, reservoir-induced landslide problems have received particular attention  
41 from engineers and geologists (Barla, 2013; Mantovani and Vitafinzi, 2003; Wolter et al., 2016).

42 For flood control and hydropower generation, one of the largest civil engineering projects in  
43 human history—the Three Gorges Water Conservation and Hydropower Project in China—was  
44 constructed and completed in 2008. Subsequently, the reservoir water level exhibited a cyclical  
45 fluctuation of 30 m (145–175 m) under normal operating conditions, and resulted in a 660-km long  
46 and 1.2-km wide (on average) hydro-fluctuation belt in the Three Gorges Reservoir (TGR) region  
47 extending from Yichang City to the Chongqing Municipality, China (Fig. 1a). Owing to the  
48 complex geological environment, climate condition, and reservoir operation, the TGR region has  
49 developed into a landslide-prone area (Wang et al., 2016), where more than 5000 reservoir-induced  
50 landslides have been identified since the first trial impoundment in 2003 (Jian et al., 2009, Yin et al.,  
51 2016, Miao et al., 2014). Studies regarding the trigger mechanisms and factors, deformation  
52 characteristics, and motion modes of reservoir-triggered landslides have been published widely  
53 (Sun et al., 2016b; Jian et al., 2009; Hu et al., 2015; Chen et al., 2015). Among the reservoir  
54 landslides, problems concerning reactivated ancient landslides including reasons for landslide  
55 reactivation, risk of a fast sliding, and available emergency civil protection actions have received  
56 significant attention, and were investigated once the old instability was identified, e.g., the Quchi  
57 landslide (Gu et al., 2017), Huangtupo landslide (Wang et al., 2016), Anlesi landslide (Jian et al.,  
58 2009), and Zhujiading landslide (Hu et al., 2015).



59 However, the clarification of the reservoir ancient landslide formation mechanism, evolution  
 60 process, and identification evidence are difficult and challenging because such instabilities vary in  
 61 size, type, disaster-pregnant setting, and formation age (Zhao et al., 2016). In fact, many  
 62 reservoir-induced old landslides were formed thousands of years ago and have been subjected to  
 63 long-term reconstructions or sediment covers; further, the original landslide geomorphic features  
 64 were blurred and modified (Deng et al., 2017; Zhao et al., 2016; Zhang et al., 2018). Such  
 65 landslides have hardly been identified owing to significant changes in the original features and  
 66 failure topography. Many researchers have studied the formation and development characteristics  
 67 based on geological processes (Cruden and Varnes, 1996), the evolution of river valleys (Xu et al.,  
 68 2008; Yin et al., 2010; Zhao et al., 2007), paleoclimatology (Xie et al., 1992; Yin et al., 2010).  
 69 However, the understanding and cognition on ancient landslides are rather superficial because of  
 70 the concealment of ancient landslides, the complexities of their formation mechanism, and the  
 71 limitations of research methods (Zhang et al., 2018).

72 The objective of this study is to investigate the formation mechanism and multi-translational  
 73 process of the Outang ancient landslide through a combined analysis of field investigation,  
 74 geological exploration, and Electron Spin Resonance (ESR) experiments. We anticipate that this  
 75 study will provide some important insights into the deposit characteristics of the old instability, as  
 76 well as the corresponding identification signs.

## 77 **Regional geological background**

78 The Outang landslide (Fig. 1c), a giant reactivated ancient landslide, is located in Anping town  
 79 of Fengjie County, Chongqing Municipality, China, and is approximately 177 km upstream of the  
 80 Three Gorges Dam (Fig. 1a). This landslide area belongs to a secondary tectonic unit of the upper  
 81 Yangtze platform, which is situated on the intersection between the Daba Mountain  
 82 bow-like folding belt and the east Sichuan folding belt. The strike of geological structures in the  
 83 study area (marked by rectangle in Fig. 1a and mapped in Fig. 1b) is dominated by the NE–SW  
 84 direction. The engineering geology map of the Outang landslide is shown in Fig. 2a. The climate in  
 85 the study area belongs to the monsoon of the subtropical moist climate zone with recognizable four  
 86 seasons. The average annual air temperature and rainfall are 16.3 °C and 1147.9 mm, respectively.  
 87 Rainfall is always concentrated in June to September annually and accounts for approximately 70%



88 of the total annual rainfall in this period.

## 89 **Overview of Outang landslide**

### 90 **Spatial geomorphological features**

91 The Outang Landslide, characterized by a reclining bell-shaped surface topography with a  
 92 maximum length of 1.8 km and a thickness of about 50.8 m, is located at the south bank of the  
 93 Yangtze River and approximately 12 km upstream away from the Fengjie urban area (Fig. 1b). The  
 94 instability deposit covers an area of 1.78 km<sup>2</sup> with an estimated volume of  $9.0 \times 10^7$  m<sup>3</sup>. It extends  
 95 from the front elevation of 90–102 m above sea level (a.s.l.) to the crown elevation of 705 m a.s.l.  
 96 along a 75–80° direction from the flow direction of the Yangtze River. The primary slide direction  
 97 is about 345°. After a careful observation, a chair-like geometry, characterized by a flat and broad  
 98 terrain at the front section but steep terrain at the middle and upper sections, occurred repeatedly  
 99 from the water level to the rear part of the landslide in spatial morphology. As illustrated in Fig. 3a,  
 100 a slope gradient of 5–10° appears and distributes at the elevation ranging from 160 m a.s.l. to 220  
 101 m a.s.l., where Anping town is located and the Fengjie–Anping road runs through; subsequently,  
 102 the steep slope, extending to about 320 m a.s.l., occurs with the slope gradient of 20–35°  
 103 (occasionally up to 50°). Another flat area (Fig. 3c), located at the elevation of roughly 330 m a.s.l.,  
 104 and a cliff (Fig. 3b, the frontal boundary of subzone O2 and mentioned in the chapter 4.2), were  
 105 recognized. Similarly, at the altitude of approximately 428–450 m a.s.l., a flat area with a slope  
 106 gradient of 2–10° (Fig. 3e) and a cliff (Fig. 3d, the frontal boundary of subzone O3 and mentioned  
 107 in the chaptered 4.3) were also identified. The spatial geomorphological features imply that the  
 108 Outang landslide might be composed of multiple landslides.

### 109 **Lithostratigraphy survey**

110 The lithostratigraphy of the landslide was studied through geological explorations and field  
 111 observations. The mobilized materials can be divided into two layers: shallow colluvium in the  
 112 top and fractured sandstone in the deep: 1) The top layer is a mixture of clayey soil and rock  
 113 blocks (approximately 25–66% volume content, sandstone, and siltstone) of sizes of 1–40 cm (Fig.  
 114 4a). Its thickness (0.2–35 m) is increased gradually toward the toe. 2) Deep in the landslide body,  
 115 the primary material is a fractured sandstone layer (Fig. 4b) with varying thicknesses between 10  
 116 m and 95 m (occasionally exceeding 110 m at the toe) and is cut intensely by two sets of fissures,



117 whose orientations follow  $120\text{--}150^\circ/55\text{--}75^\circ$  (dip/dip angle) and  $40\text{--}70^\circ/60\text{--}85^\circ$ . Trench and adit  
 118 explorations disclosed that dark gray claystone and clayed soil (coal and shale can also be found  
 119 occasionally) are predominant at three weak interlayers (WIs) with a thickness of 5–20 cm (Fig.  
 120 4c). The bedrock at the attitude of  $335\text{--}350^\circ/18\text{--}24^\circ$  (dip/dip angle) are constituted by  
 121 sublitharenite of the Xujiahe formation in the Upper Triassic system ( $T_{3xj}$ ) and fine sandstones of  
 122 the Zhenzhuchong formation in the Lower Jurassic system ( $J_{1z}$ ), with the former overlain by the  
 123 latter (Fig. 3a). As shown in Fig. 4d, bedding planes that indwell in the outcrops of the bedrock  
 124 (sandstone) at the rear part develop a downslope with the attitude of  $336^\circ/18^\circ$ .

#### 125 **Weak interlayers**

126 The presence of a shear plane is often assumed as evidence of a slip surface (Hutchinson and  
 127 Bhandari, 1971; Corominas et al., 2005). In-site investigation found three WIs (numbered WI1,  
 128 WI2, and WI3, and marked in Fig. 5a). The slip surfaces existing in the WIs were discovered with  
 129 clear striated polished surfaces by adit (WI1 in Fig. 5b) and trench explorations (WI3 in Fig. 5c).  
 130 The main mineral materials in the WIs are quartz and clay minerals with the average contents of  
 131 more than 35.2% and 44.7%, respectively. Additionally, the clay minerals, composed of  
 132 montmorillonite (up to 74%), illite (15%–31%), and kaolinite (5%–11%) are characterized by high  
 133 swelling, softening potential, and low permeability. To clarify the apparent age of the Outang  
 134 landslide, the ESR experiment was conducted and eight samples near the slip surface were  
 135 prepared using a drilling hole, trench, and adit explorations (marked in Fig. 2a). Information on the  
 136 eight samples is presented in Table 1. The ESR results indicate (in Fig. 2a) that the apparent age of  
 137 the Outang landslide can be subdivided into 120–130 ka for the low part, 65–68 ka for the  
 138 middle part, and 47–49 ka for the upper part, thus proving that the ancient instability could be  
 139 composed of several independent landslides.

#### 140 **Activity signs**

141 Since the first trial impoundment, the instability activity features have become increasingly  
 142 obvious. At the low part, most of its volume is submerged by the reservoir water owing to its  
 143 low-flat terrain and local collapse, and failures were observed in the reservoir water fluctuation  
 144 zone frequently. Figure 6b illustrates the representative local collapse with a material of volume of  
 145  $2.3 \times 10^4 \text{ m}^3$  sliding into the river, and the front boundary of the landslide retreated nearly 6 m with



146 some falling sandstone blocks observed on the slope surface. The movement has also resulted in  
 147 some damages in the Anping town houses (Fig. 6c). At the middle part, a long tension crack of  
 148 length 74.5 m, width 0.1–75 cm, and visible depth 10–110 cm was observed at an altitude between  
 149 350 m and 370 m a.s.l. (Fig. 6d). Meanwhile, the dislocation and cracking of the road at a few  
 150 places were identified. For example, Fig. 6e shows a typical dislocation with the maximum  
 151 dislocation of 0.5 m. At the upper part, many signs of reactivation were also exhibited. A fallen  
 152 telegraph pole was found as a consequence of the continuous surficial movement (Fig. 6f); the  
 153 newly installed telegraph pole was inclined downslope at an angle of 12° (Fig. 6f). The upslope  
 154 boundary of the instability is defined by a scarp, where WI3 was exposed (Fig. 6g).

#### 155 **Accumulation characteristics of active parts**

156 In terms of the spatial geomorphology features, ESR results, and slip surface morphology, the  
 157 Outang ancient landslide can be divided into three independent reactivated subzones (labeled  
 158 subzones O1, O2, and O3). Generally, the component of the mobilized material in each subzone is  
 159 similar with that of the top layer is shallow colluvium material (clayey soil and rock blocks), and  
 160 the deep layer is fractured sandstone. The fractured sandstone structure is spoon like, characterized  
 161 by an orientation of stratified or stratoid bedding planes (335–350°/18–24°) from the rear to  
 162 mid-fore part; it changes to nearly horizontal, and curves upward at the toe area (155–170°/0–15°)  
 163 in each subzone. For example, the orientation of the bedding planes within the fractured sandstone  
 164 is 340°/21° (Fig. 7b), but changes to 162°/15° (Fig. 4b). Moreover, the variation rule of the  
 165 fractured sandstone structure in each subzone is similar to its respective slip surface morphology.

#### 166 **Subzone O1**

167 Located at the low part of the landslide, subzone O1 has a reclining bell-shaped surface  
 168 geometry with a primary slip direction of roughly 345° (Fig. 2a). The elevation of the frontal part of  
 169 subzone O1 is approximately 90–102 m a.s.l. (submerged by water completely); the crown  
 170 elevation is 300–370 m a.s.l. and is covered partly by subzone O2. It has a maximum length of 880  
 171 m, a width of 1100 m, and an average thickness of 70.3 m. This zone has an area of  $9.22 \times 10^5 \text{ m}^2$   
 172 and a volume of  $6.48 \times 10^7 \text{ m}^3$ . As mapped in Fig. 7a, the shallow colluvium material has an uneven  
 173 thickness of 10 to 35 m; the layer of fractured sandstone exhibits an average thickness of 62 m. Two  
 174 local strong deformation areas distributed at both sides of the toe of O1 (mapped in Fig. 2a) were



clarified with a total volume of  $4.1 \times 10^6 \text{ m}^3$ . Slip surfaces with clear sliding traces for the two local strong deformation areas were also revealed by geological exploration (Fig. 7c–d). Moreover, adit exploration revealed that the slip surface of this subzone existed in W11, where the main components were claystone (size of 0.5–6 cm) and clayed soil (content of 60–80%), whose colors are dark gray and gray, respectively (Fig. 4c).

#### Subzone O2

Subzone O2 is located at the middle of the landslide. It extends from 250–300 m at its toe to 400–530 m a.s.l. at its rear section, where it is wrapped partly by subzone O3. This zone has a length of approximately 440 m, width of 650 m, area of  $3.16 \times 10^5 \text{ m}^2$ , and volume of  $1.02 \times 10^4 \text{ m}^3$ . As illustrated in Fig. 8a, the thickness of the deposit material in this subzone is approximately 32 m, and the thickness of the shallow colluvium is less than 6 m. The slip surface of subzone O2 also exists in W11; it was revealed by a drill hole (numbered 5 in Table 1) of thickness 3–15 cm and was dark gray. The field investigation shows a cliff with a vertical dislocation of 8.5 m, and the exposed fractured sandstone is the frontal boundary of this subzone (bounded in Fig. 3a and illustrated in Fig. 3b); the lateral boundary is a ridge in the west (Fig. 1c and Fig. 3c) and a gully in the east (Fig. 1c). Owing to the blockage of the rear part of subzone O1, the flat area appears at the mid-fore part of subzone O2 (marked in Fig. 3a and displayed in Fig. 3c). The ESR experiment shows that the apparent age of subzones O1 and O2 are 120–130 ka and 65–68 ka, respectively, indicating that both subzones occurred at different times; specifically, subzone O2 occurred later than subzone O1.

#### Subzone O3

Subzone O3 was seated at the upper part of the Outang landslide with a length of 0.64 km, width of 0.83 km, and an average thickness of 27.2 m that increased downslope. It extends from 400–530 m a.s.l. to 705 m a.s.l., with an entire planar area of  $0.54 \text{ km}^2$  and a volume of  $1.45 \times 10^7 \text{ m}^3$ . The shallow colluvium is extremely thin (less than 1.2 m, as shown in Fig. 7a). Cliff daylighting with broken rock mass and bloating with many shear and tension-shear cracks was found at an altitude of roughly 408 m a.s.l., which is the frontal boundary of this subzone (labeled in Fig. 3a and illustrated in Fig. 3d). The flat area located at the mid-fore part of subzone O3 was also recognized (marked in Fig. 3a and shown in Fig. 3e). Trench exploration disclosed that the



204 slip surface of this subzone existed in WI3, where the dominated component was carbonaceous  
 205 claystone (size of 2–18 mm and content of 75%) and dark-gray clayed soil of thickness 8–20 cm  
 206 (Fig. 4c). Moreover, the rear part of this subzone is bounded by the scarp of the daylighting of WI3  
 207 (Fig. 6g). The ESR experiment indicates that the apparent age of subzone O3 is the latest  
 208 compared to that of subzones O2 and O1.

## 209 Discussion

### 210 Mechanism and process

211 Based on the investigation and analysis of the basic characteristics of the Outang landslide, and  
 212 in conjunction with the information about the engineering geology and ESR experiments, a  
 213 conceptual model for understanding the formation mechanism and multistage sliding process of  
 214 this instability is deduced and shown in Fig. 8. The detailed descriptions of these processes are as  
 215 follows:

- 216 1. At the stage of Early Pleistocene, the whole TGR has suffered from intermittent uplift, tilt,  
 217 and continuous action of intensive river incision (the fluvial incision rate up to 92.5 cm/ka  
 218 between the river section of Chongqing and Fengjie) as the effect of the Himalayas'  
 219 movement, causing the appearance of steep-sided valleys that provided space for the slope  
 220 movement (Fig. 8a–b).
- 221 2. A weak interlayer (WI1), and some tectonic and weathering cracks within the rock mass  
 222 occurred. During heavy rainfall, rainwater could penetrate the rock mass along the cracks  
 223 and converge to the WI1. On one hand, the WI1 would suffer from the action of softening  
 224 or argillation, and then slip or squeeze out to the free surface (Zhao et al., 2012). On the  
 225 other hand, hydrostatic pressure caused by water flow could induce a larger uplift pressure  
 226 (Zhao et al., 2015). Both factors contribute to the overlying rock stratum creep–slide along  
 227 WI1 and result in tensile cracks (Fig. 8b). Because WI1 is not exposed at the lowest part of  
 228 the slope, where the sliding resistance mass is strong, stress will be concentrated at the toe  
 229 area of the slope because of the slope creep deformation, thus resulting in a slight bending  
 230 and upward uplift of the rock stratum at this part (bounded by rectangle in Fig. 8b).
- 231 3. Under the combined action derived from long-term precipitation infiltration and gravitation,  
 232 the creep deformation of the rock stratum above WI1 is successive, thus widening the





233 tensile crack and extending it toward W11 (Fig. 8c). Additionally, the fracture and flexure  
 234 upward of the rock mass become increasingly acute at the toe, accompanied by numerous  
 235 fissures and relaxed rock mass (bounded by rectangle in Fig. 8c). The orientation of the  
 236 fractured sandstone next to the toe area (Fig. 4b) of subzone O1 is the best evidence to  
 237 justify the processes of bend and fracture of the rock stratum. These processes further  
 238 cause rainwater to seep into the slope easily and generate a potential curved shear surface  
 239 with a tendency to join with the W11 gradually (Fig. 8c).

240 4. As time progressed and owing to the infiltration of rainwater, the tensile structural plane  
 241 and potential curved shear surface became gradually connected with W11. Approximately  
 242 120–130 ka ago, as induced by heavy rain and other factors, a translational landslide  
 243 (subzone O1) occurred along the shear rupture surface (slip surface) (Fig. 8d). Thus, the  
 244 formation mechanism of subzone O1 can be summarized as slide–bending. During the  
 245 sliding process, under the influence of the reservoir buttress effect (circled in Fig. 8d)  
 246 (Paronuzzi et al., 2013) and slip surface morphology (Fletcher et al., 2002; Sun et al.,  
 247 2016), the moved subzone O1 stopped progressively.

248 5. After the generation of subzone O1, a new free surface (Fig. 8d) occurred at the front of the  
 249 rock stratum at the middle part of the slope consequent, where W11 is exposed. The  
 250 mechanical property of W11 would further deteriorate under the adverse effect of water;  
 251 moreover, the rock stratum at the middle part exhibits a large tendency to move along W11  
 252 on account of the long-term gravitational deformation (Deng et al., 2017). Approximately  
 253 65–68 ka ago, another translational landslide (subzone O2) was induced along W11 (Fig.  
 254 8e). Therefore, the formation mechanism of subzone O2 can be summarized as a planar  
 255 slide.

256 Owing to the blockage of subzone O1, the moving subzone O2 gradually stopped with  
 257 the rear area of subzone O1 being covered by subzone O2. In this process, part of the  
 258 moving rock mass at the front part of subzone O2 is crushed, and accumulates along the  
 259 slope surface of subzone O1, whereas most parts of the rock stratum remain on the slope  
 260 and/or hang in air (circled in Fig. 8e). Moreover, controlled by the slip surface morphology  
 261 and hindrance of the rear part of subzone O1, the dip of the rock stratum at the front part



262 of subzone O2 is typically opposite to that of the slope, and the flat topographical area can  
 263 been recognized (Fig. 3c).

264 6. The phenomena of unloading, rebound, and attenuated sliding resistance mass at the toe of  
 265 the upper part of the slope are inevitable after the emergence of subzone O2; they are in  
 266 favor of the creep deformation of the upper part of the slope above WI3 and give rise to  
 267 the bending and upward uplift of the rock stratum at the toe of this part (bounded in Fig.  
 268 8e). When the possible rupture surface was created and connected with WI3 gradually, as  
 269 induced by heavy rain and other factors, a landslide (subzone O3) occurred (47–49 ka ago  
 270 (Fig. 8f)). The formation process of subzone O3 is similar to that of subzone O1; the  
 271 formation mechanism can be classified as slide–bending. Moreover, for the reason of the  
 272 blockage of subzone O2, the moving subzone O3 gradually stopped with the rear area of  
 273 subzone 2 covered by subzone O3. The structure of the rock stratum and its morphological  
 274 features are also similar to those of subzone O2, as well as a flat topography area can also  
 275 be found (Fig. 3e).

276 For subzone O1, after the landslide, a relatively stable period characterized by a thicker top  
 277 layer formed, and the morphology and location of the frontal boundary changed due to the humid  
 278 and rainy climate (Fig. 2a and/or Fig. 6a). For subzones O2 and O3, the rock stratum that is pushed  
 279 out is suspended without support at its bottom (Figs. 8e–f). Owing to its own gravity and the  
 280 weather, local cracking and the collapse failure of rock mass occurred; this may explain the  
 281 occurrences of cliffs with large dip angles and many fissures at the front parts of subzones O2 and  
 282 O3 (labeled in Fig. 2a and shown in Fig. 2b and Fig. 2b, respectively). Meanwhile, the failed mass  
 283 would move downslope and accumulate on the slope surface; this may have caused the thickness of  
 284 the top layer for each subzone to follow the order of  $O1 > O2 > O3$ . Another reason may be the  
 285 apparent age; this implies that the earlier the subzone occurs, the thicker is the top layer. For the  
 286 Outang landside, the earliest is subzone O1, followed by subzone O2 and then the latest is the  
 287 subzone O1. Overall, with the evolution of the Yangtze River, the long-term geologic force has  
 288 evidently changed the features of the original slope. Hence, the Outang landslide is an ancient  
 289 landslide that has experienced the long process of sliding, bending, accumulating, and remolding.

290 **Identification evidence**



291 Since the occurrence of the old landslide, it has undergone a long-term geological  
 292 transformation (human activities, weathering, erosion, etc.). Consequently, many original landslide  
 293 characteristics have vanished, and the original topography and geomorphology have varied, thus  
 294 causing significant difficulties in landslide identification (Zhao et al., 2015). However, in the  
 295 specific case of the Outang ancient landslide, some evidences remain that can be used to identify  
 296 such an old instability.

#### 297 1. Mobilized material structure characteristics and slip surface

298 The landslide is located at the southeast wing of the Guling syncline, where the orientation of  
 299 the bedrock is  $335\text{--}350^\circ/18\text{--}24^\circ$ . The dip in the bedding planes within the mobilized materials is  
 300 the same as that of the bedrock from the rear to the mid-fore ( $335\text{--}350^\circ$  in Fig. 7b), but opposite to  
 301 that of the bedrock at the toe of each subzone ( $155\text{--}170^\circ$  in Fig. 4b). This implies that the attitude  
 302 of the mobilized material is variable, as characterized by the dip angle decreased nearly horizontal  
 303 and curved upward at the toe of each subzone, which is analogous to its respective slip surface.  
 304 The slip surface, particularly of the striated polished surface, interpreted as a result of relative  
 305 displacements among the displaced materials and the bedrock, was revealed by geological survey  
 306 (Fig. 5b–c) with the orientation similar to that of the mobilized material. Thus, the material  
 307 structure characteristic and rupture surface are strong and clear evidences for identifying the  
 308 ancient landslide.

#### 309 2. Landform characteristics

310 As previously mentioned, the Outang landslide has experienced the long process of remodeling  
 311 with a steep topography (varies from  $20^\circ$  to  $45^\circ$ ) under the elevation of 160 m a.s.l.; however, it  
 312 changes to  $5\text{--}10^\circ$  immediately at the altitude of 160–220 m a.s.l. with the occurrence of a flat and  
 313 broad area (a slope of  $5\text{--}10^\circ$ ), where human activities (e.g., building roads (Fengjie–Anping road)  
 314 and reclamation projects (Anping Town)) were frequent and intensive. Analogously, two cliffs at  
 315 the elevation of about 290 m a.s.l. and 462 m a.s.l. (Fig. 3b and Fig. 3d, respectively), and the flat  
 316 terraces at the mid-fore parts of O2 and O3 (Fig. 3c and Fig. 3e, respectively) have attracted a  
 317 substantial amount of attention, thus rendering the landslide area significantly different from the  
 318 surrounding mountains and easily recognized. Thus, topography saltation occurring in the  
 319 landslide area will be the important evidence of landslide identification in field investigations.



### 320 3. Underground water characteristics

321 For the Outang landslide, many cracks distributed at the ground surface provided better access  
 322 for rainfall infiltration. As shown in Fig. 7a, the thickness of mobilized materials decreased  
 323 substantially (less than 1.2 m for shallow materials and approximately 26 m for the fractured  
 324 sandstone layer at sliding mass O3). Moreover, the permeability for the fractured sandstone is large  
 325 (roughly  $3.35 \times 10^{-3}$  cm/s). These factors allow rainwater to sweep easily into the rock mass, thus  
 326 causing increasing underground water level that appear in the form of a spring at the front part of  
 327 each subzone. Typically, this type of spring is characterized by a large flow during the heavy  
 328 rainfall season (Fig. 9a) that decreases substantially during the dry season (Fig. 9b).

### 329 Evolution of stability

330 The earliest geological survey report, provided by the Sichuan Geology and Mineral Bureau in  
 331 August 1988, indicated that the Outang landslide is stable or quasi-stable, which was further  
 332 confirmed by the Comprehensive Survey Bureau of the Yangtze Water Resources Committee in  
 333 December 1995. However, the deformation and failure of old landslide have been discovered  
 334 frequently and have received particular attention by local residents and authorities; therefore, a  
 335 landslide disaster prevention project (installing anti-slide piles, etc. labeled in Fig. 2a and mapped  
 336 in Fig. 2b) was proposed by the Yangtze Institute of Survey, Planning, Design, and Research, and  
 337 was completed in November 2003. Since then, landslide stability has been improved significantly.  
 338 Unexpectedly, after the TGR dam was completed in 2008, the landslide reactivated signs,  
 339 including the damage of houses and roads, broadening of cracks, failure of local collapse, etc.,  
 340 were increasingly evident. Meanwhile, striated polished surfaces were also discovered by  
 341 geological exploration, and two local strong deformation areas with a total volume of  $4.1 \times 10^6$  m<sup>3</sup>  
 342 distributed at both sides of the toe of O1 was recognized as well. Thus, the landslide stability  
 343 decreased substantially and exhibited the tendency of a complete failure, as reported in November  
 344 2012. Although another remediation project, including backfill toe weight and lattice revetment in  
 345 the east strong-deformation area (bounded in Fig. 2a and shown in Fig. 2c) and masonry revetment  
 346 in the west strong-deformation area (marked in Fig. 2a and demonstrated in Fig. 2d), was  
 347 completed in 2013, the landslide is in a state of continuous creep deformation with increasingly  
 348 evident activity signs hitherto (including road and house damages, ground fissures, local collapses,



etc.). Further, the landslide stability is ambiguous (Huang and Luo 2018, under review).

## Conclusion

The Outang landslide could be divided into three subzones with an apparent age of 120–130 ka for subzone O1, 65–68 ka for subzone O2, and 47–49 ka for subzone O3, among which the change rules of the deposit material attitude in each subzone were similar and the same to its respective slip surface morphologies. Additionally, two local strong deformation areas were identified at both sides of subzone O1.

This landslide deposit has evolved from multiple ancient translational sliding masses with the formation mechanism of slide–bending for subzones O1 and O3, and planar sliding for subzone O2. Moreover, the local collapse and accumulation downslope, and the apparent age of each subzone could be the reasons for the change in the thickness of the top layer.

The material structure characteristics, rupture surface, topography saltation, and seasonal variation of groundwater exposure could be regarded as valid proofs in identifying ancient landslides during an on-site investigation.

Currently, although the landslide has undergone two remedial measures, its stability remains uncertain based on the significant landslide deformation and reactivated features. Therefore, long-term monitoring and emergency civil protection actions are necessary.

## Acknowledgments

This work is supported by the Fundamental Research Funds for the Central Universities (No. 106112017CDJXSY002), the Graduate Research and Innovation Foundation of Chongqing, China (No. CYB17043), the National Natural Science Foundation of China (Nos. 41672300, 41472245 and 51578091), and Open Research Fund Program of Hunan Province Key Laboratory of Safe Mining Techniques of Coal Mines (No. E21831).

## References

- Barla, G.: The 1963 Vajont Landslide: 50th Anniversary, *Rock Mechanics and Rock Engineering*, 46, 1267–1270, 2013.
- Chen, M. L., Lv, P. F., Zhang, S. L., Chen, X. Z., and Zhou, J. W.: Time evolution and spatial accumulation of progressive failure for Xinhua slope in the Dagangshan reservoir, Southwest China, *Landslides*, 15, 565–580, 2015.
- Corominas, J., Moya, J., Ledesma, A., Lloret, A., and Gili, J. A.: Prediction of ground displacements and velocities from groundwater level changes at the Vallcebre landslide



- 380 (Eastern Pyrenees, Spain), *Landslides*, 2, 83–96, 2005.
- 381 Cruden, D. M., and Varnes, D. J.: Landslide types and processes, special report, transportation  
382 research board, National Academy of Sciences, 247, 36–75, 1996.
- 383 Deng, H., Wu, L. Z., Huang, R. Q., Guo, X. G., and He, Q.: Formation of the Siwanli ancient  
384 landslide in the Dadu River, China, *Landslides*, 14, 385–394, 2017.
- 385 Deng, Q., Min, F., Ren, X., Liu, F., and Tang, H.: Precedent long-term gravitational deformation of  
386 large scale landslides in the Three Gorges reservoir area, China, *Engineering Geology*, 221,  
387 170–183, 2017.
- 388 Fletcher, L., Hungr, O., and Evans, S. G.: Contrasting failure behaviour of two large landslides in  
389 clay and silt, *Revue Canadienne De Géotechnique*, 39, 46–62, 2002.
- 390 Gu, D. M., and Huang, D.: A complex rock topple-rock slide failure of an anacinal rock slope in the  
391 Wu Gorge, Yangtze River, China, *Engineering Geology*, 208, 165–180, 2016.
- 392 Gutiérrez, F., Linares, R., Roqué, C., Zarroca, M., Carbonela, D., Rosell, J., and Gutiérrez, M.:  
393 Large landslides associated with a diapiric fold in Canelles Reservoir (Spanish Pyrenees):  
394 Detailed geological-geomorphological mapping, trenching and electrical resistivity imaging,  
395 *Geomorphology*, 241, 224–242, 2015.
- 396 Hu, X., Zhang, M., Sun, M., Huang, K., and Song, Y.: Deformation characteristics and failure mode  
397 of the Zhujiadian landslide in the Three Gorges Reservoir, China, *Bulletin of Engineering  
398 Geology and the Environment*, 74, 1–12, 2015.
- 399 Huang, D., Luo, S. L.: (Interpreting the deformation and reactivated mechanism of a giant  
400 translational ancient landslide in the Three Gorges Reservoir, China”, *Landslides*, under review,  
401 2018)
- 402 Huang, D., Gu, D. M., Song, Y. X., Cen, D. F., and Zeng, B.: Towards a complete understanding of  
403 the triggering mechanism of a large reactivated landslide in the Three Gorges Reservoir,  
404 *Engineering Geology*, 238, 36–51, 2018.
- 405 Huang, D., and Zhu, T. T.: Experimental and numerical study on the strength and hybrid fracture of  
406 sandstone under tension-shear stress, *Engineering Fracture Mechanics*, 200, 387–400, 2018.
- 407 Hutchinson, J. N., and Bhandari, R. K.: Undrained loading, a fundamental mechanism of mudflows  
408 and other mass movements, *Geotechnique*, 21, 353–358, 1971.
- 409 Jacobs, L., Dewitte, O., Poesen, J., Sekajugo, J., Nobile, A., Rossi, M., Thiery, W., and Keryn, M.:  
410 Field-based landslide susceptibility assessment in a data-scarce environment: the populated  
411 areas of the Rwenzori Mountains, *Natural Hazards and Earth System Sciences*, 18, 1–31, 2018.
- 412 Jian, W., Wang, Z., and Yin, K.: Mechanism of the Anlesi landslide in the Three Gorges Reservoir,  
413 China, *Engineering Geology*, 108, 86–95, 2009.
- 414 Liu, B., Siu, Y., and Mitchell, G.: Hazard interaction analysis for multi-hazard risk assessment: a  
415 systematic classification based on hazard-forming environment, *Natural Hazards and Earth  
416 System Sciences*, 16, 629–642, 2016.
- 417 Mantovani, F., and Vitaforzi, C.: Neotectonics of the Vajont dam site, *Geomorphology*, 54, 33–37,  
418 2003.
- 419 Miao, H., Wang, G., Yin, K., Kamai, T., and Li, Y.: Mechanism of the slow-moving landslides in  
420 Jurassic red-strata in the Three Gorges Reservoir, China, *Engineering Geology*, 171, 59–69,  
421 2014.
- 422 Paronuzzi, P., Rigo, E., and Bolla, A. I.: Influence of filling-drawdown cycles of the Vajont











- 423 Reservoir on Mt. Toc slope stability, *Geomorphology*, 191, 75–93, 2013.
- 424 Sättele, M., Bründl, M., and Straub, D.: Quantifying the effectiveness of early warning systems for  
425 natural hazards, *Natural Hazards and Earth System Sciences*, 16, 149–166, 2016.
- 426 Sun, G., Zheng, H., Huang, Y., and Li, C.: Parameter inversion and deformation mechanism of  
427 Sanmending landslide in the Three Gorges Reservoir Region under the combined effect of  
428 reservoir water level fluctuation and rainfall, *Engineering Geology*, 205, 133 – 145, 2016b.
- 429 Sun, G., Huang, Y., Li, C., and Zheng, H.: Formation mechanism, deformation characteristics and  
430 stability analysis of Wujiang landslide near Centianhe reservoir dam, *Engineering Geology*,  
431 211, 27–38, 2016.
- 432 Varnes, D. J.: Slope movement types and processes, *Landslides-Analysis and control: National*  
433 *Research Council*, Washington, D.C., Transportation Research Board, Special Report 176, pp.  
434 11–33, 1978.
- 435 Wang, J., Xiang, W., and Lu, N.: Landsliding triggered by reservoir operation: a general conceptual  
436 model with a case study at Three Gorges Reservoir, *Acta Geotechnica*, 9, 771–788, 2014.
- 437 Wolter, A., Stead, D., Ward, B. C., Clague, J. J., and Ghirotti, M.: Engineering geomorphological  
438 characterization of the Vajont slide, Italy, and a new interpretation of the chronology and  
439 evolution of the landslide, *Landslides*, 14, 1–15, 2016.
- 440 Xie, S. Y., Li, M. S., and Xu, W. Y.: Evolution of Huanglashi landslide in the Three Gorges  
441 Reservoir area and ancient environmental climate, *Chinese Journal of Wuhan University of*  
442 *Hydraulic and Electric Engineering*, 21, 189–192, 1999.
- 443 Xu, Q., Chen, W., and Zhang, Z. Y.: New views on forming mechanism of deep overburden on river  
444 bed in Southwest of China, *Chinese Journal of Advances in Earth Science*, 23, 448–455, 2008.
- 445 Yin, Y., Huang, B., Wang, W., Wei, Y., Ma, X., and Ma, F.: Reservoir-induced landslides and risk  
446 control in Three Gorges Project on Yangtze River, China, *Journal of Rock Mechanics and*  
447 *Geotechnical Engineering (in English)*, 8, 577–595, 2016.
- 448 Yin, Z. Q., Cheng, G. M., Hu, G. S., Wei, G., and Wang, Y. Q.: Preliminary study on characteristics  
449 and mechanism of super-large landslides in upper Yellow River since Late-Pleistocene,  
450 *Chinese Journal of Engineering Geology*, 18, 41–51, 2010.
- 451 Zhang, Y. S., Wu, R. L., Guo, C. B., Wang, L. C., Yao, X., and Yang, Z.H.: Research progress and  
452 prospect on reactivation of ancient landslides, *Chinese journal of Advances in Earth Science*,  
453 33, 728–740, 2018.
- 454 Zhao, X. T., Zhang, Y. S., Qu, Y. C., Guo, C. B.: Pleistocene glaciations along the western foot of  
455 the Yulong Mountains and their relationship with the formation and development of the Jinsha  
456 River, *Chinese Journal of Quaternary Sciences*, 27, 35–44, 2007.
- 457 Zhao, Y., Xu, M., Zhao, H. M.: Study on the critical water head in the trailing edge of translational  
458 landslide. In: 11th International and 2nd North American Symposium on Landslides, CRC  
459 press, Alberta, pp 693–698, 2012.
- 460 Zhao, Y., Xu, M., Guo, J., Zhang, Q., Zhao, H. M., Kang, X. B., and Xia, Q.: Accumulation  
461 characteristics, mechanism, and identification of an ancient translational landslide in china,  
462 *Landslides*, 12, 1119–1130, 2015.





Table 1 The information and images of eight samples

Number	Picture	Description	Sampling depth/ m	Elevation/ m a.s.l.	Method
1		Dark gray clay soil	183–183.5	270.1	Adit excavation
2		Dark gray carbonaceous claystone interbedded with coal	122–122.9	179.8	Drill hole
3		Gray argillaceous clay soil and gravel	44.5–49.2	299.3	
4		Gray claystone interbedded with shale	41.4–42.7	324.4	
5		Dark gray, gray carbonaceous claystone	32.9–33.6	415.2	
6		Gray argillaceous claystone	29.6–29.8	470.1	
7		Gray argillaceous claystone	40.8–41.1	542.9	
8		gray soil	3.2–3.5	446.2	Trench exploration



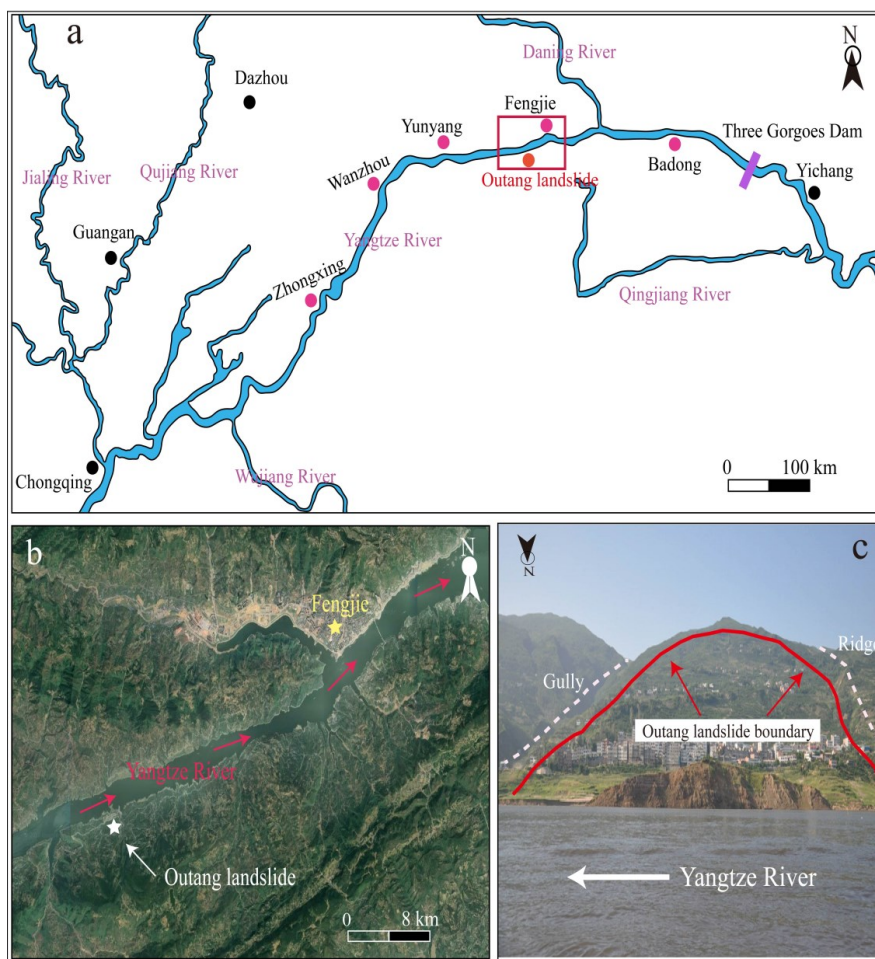


Fig. 1. Outang landslide in the Three Gorges Reservoir area. **a** The Three Gorges Reservoir area. **b** Landslide location map of the study area. **c** A closed-up view of the Outang landslide

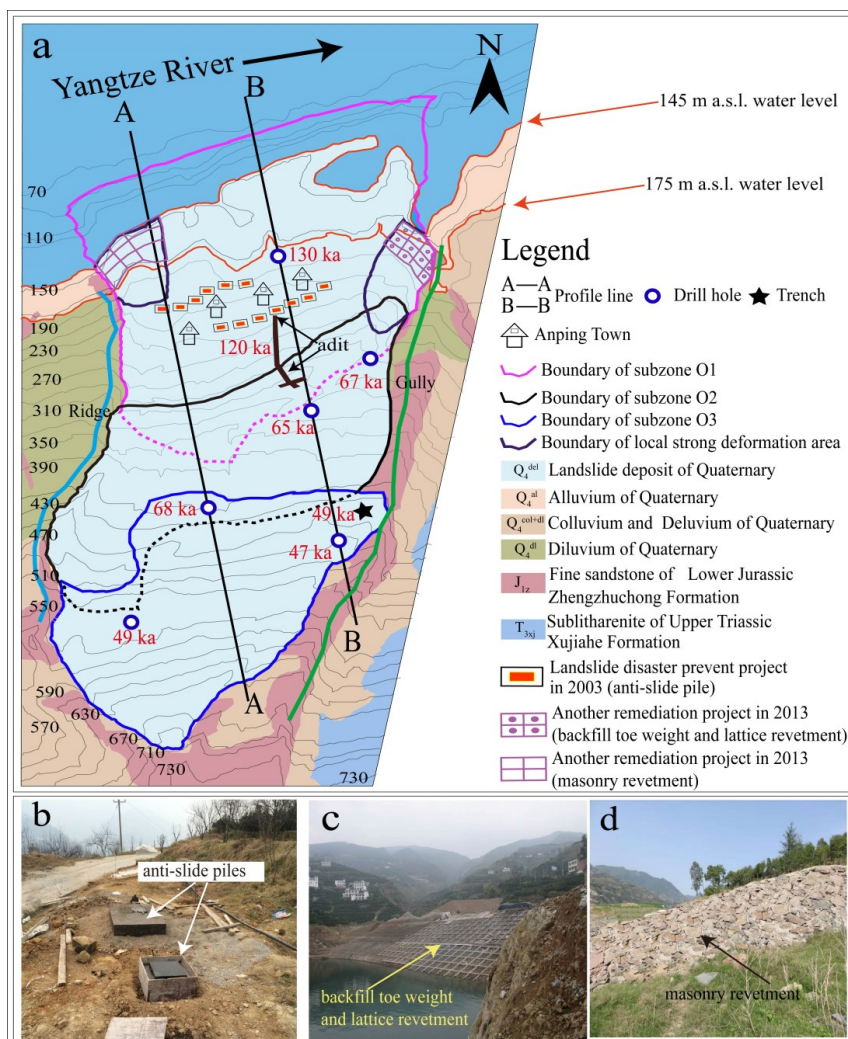


Fig. 2. Outang landslide and some pictures of landslide treatment in 2003 and 2013. **a** Engineering geological map of the landslide. **b** Partial images of the landslide disaster prevent project in 2003. **c–d** Partial photos of the landslide remediation project in 2013

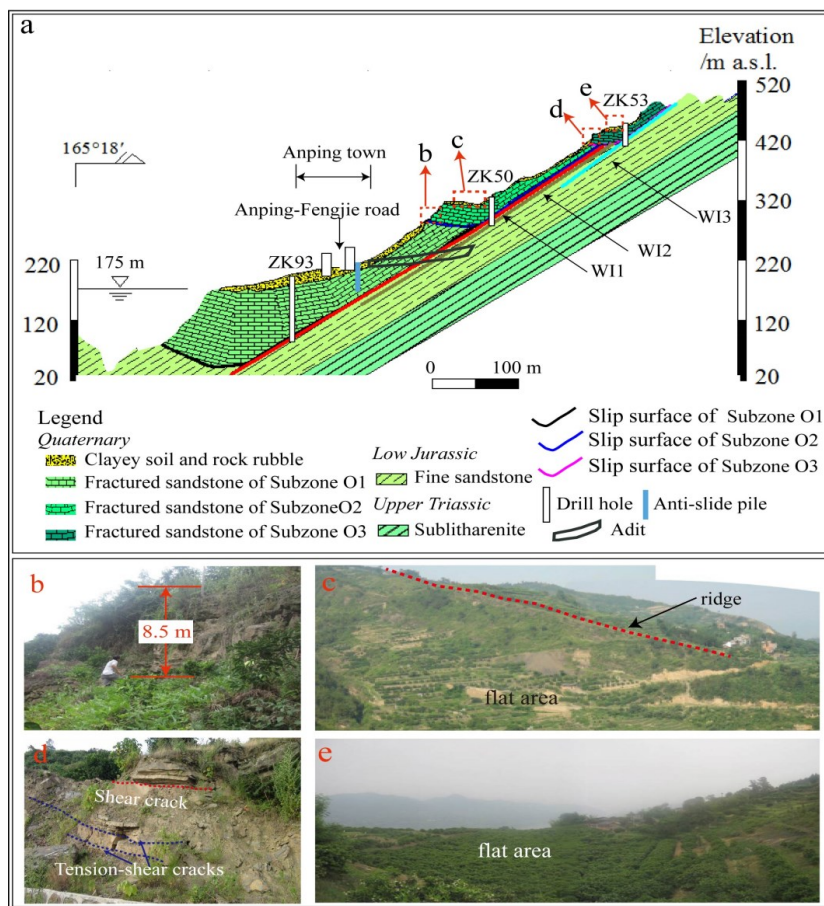


Fig. 3. Outang landslide and its geomorphological features. **a** Geological cross section B-B of the landslide (see location in Fig. 2a). **b** and **d** Partial photographs of cliffs (see location in Fig. 3a). **c** and **e** Images of flat areas (see location in Fig. 3a).

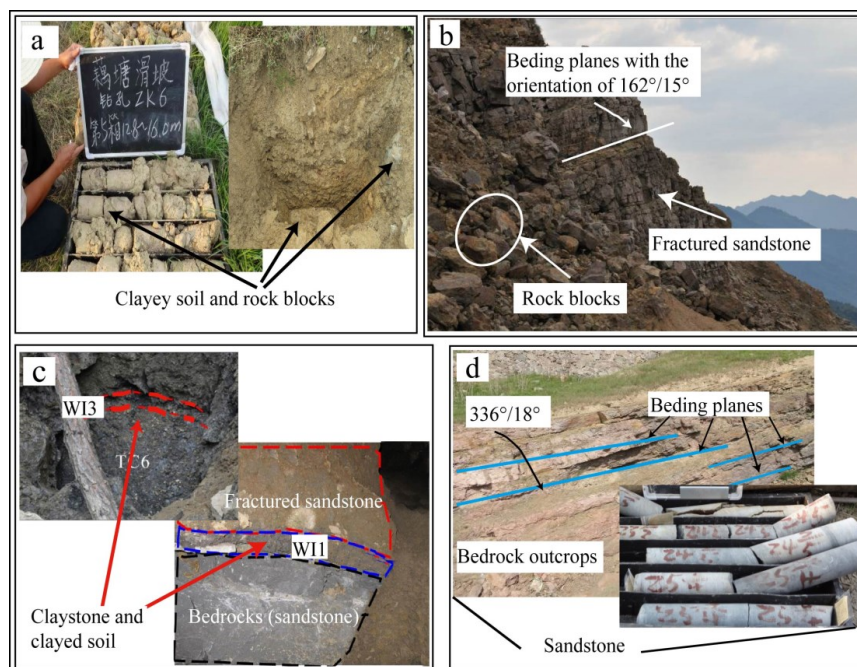


Fig. 4. Bedrock and mobilized materials of the landslide. **a** Shallow colluvium. **b** Bedding planes and rock daylighting at the of the landslide. **c** Weak interlayers revealed by adit (W11) and trench (W13) exploration. **d** Bedrock exposed by drill hole and bedding planes within the bedrock daylighting at the rear of the landslide.



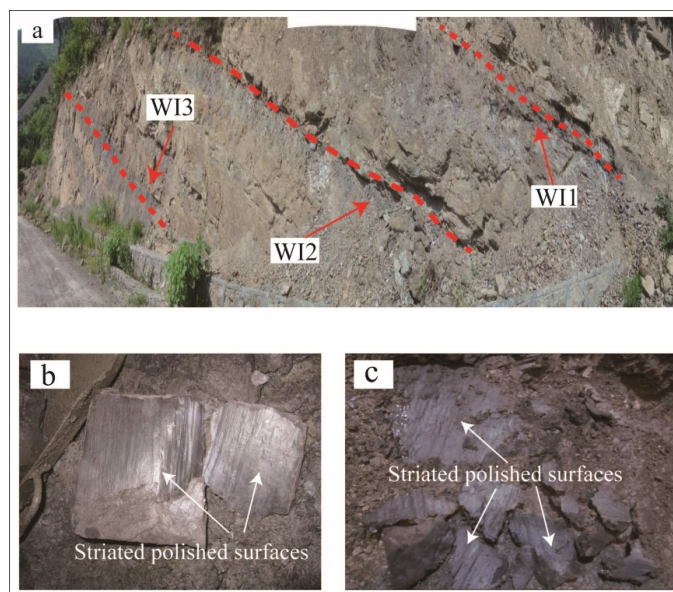


Fig. 5. Weak interlayers. **a** Weak interlayers outcrops. **b–c** Slip surfaces with striated polished surfaces revealed by adit and trench exploration

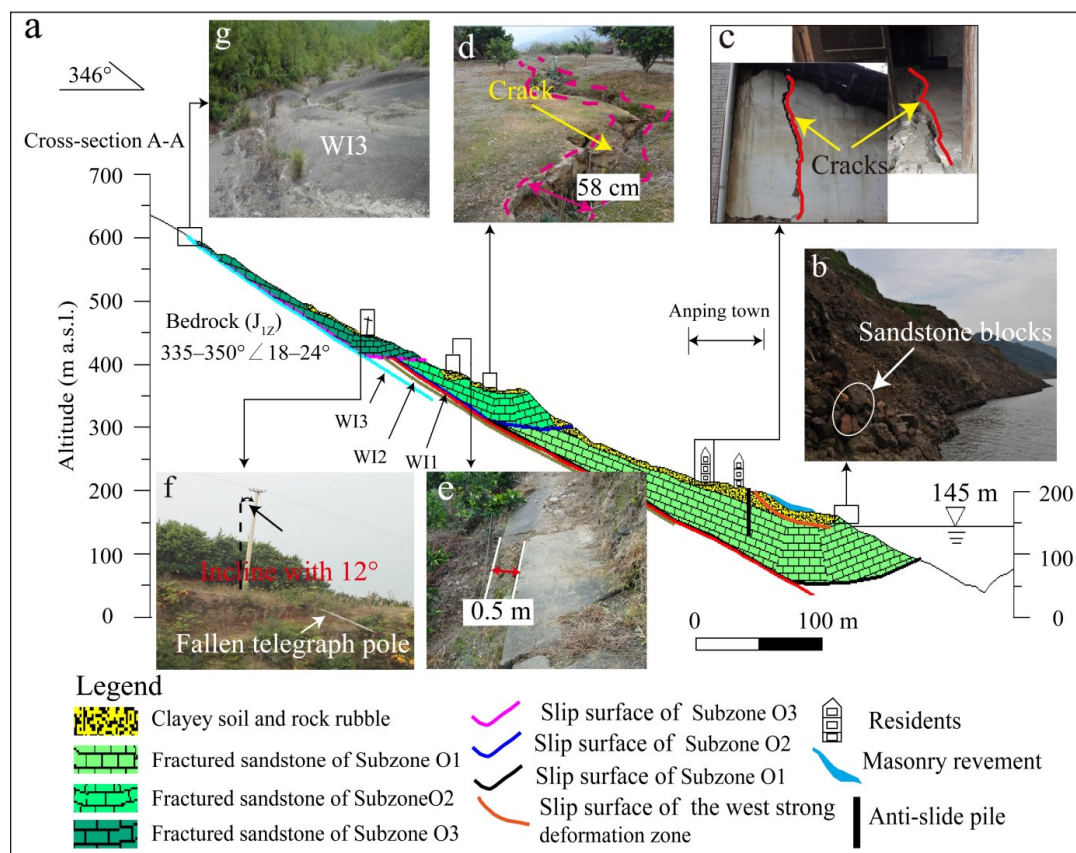


Fig. 6. Geological profile and Failure features on the surface of the Outang landslide. **a** Geological cross section A-A of the instability (see location in Fig. 2a). **b** Local collapse at the front part of the landslide. **c** Cracks on houses. **d** Cracks on ground surface. **e** Road dislocation. **f** Fallen and inclined telegraph pole. **g** Scrap with the exposure of W13 at the rear part of the instability

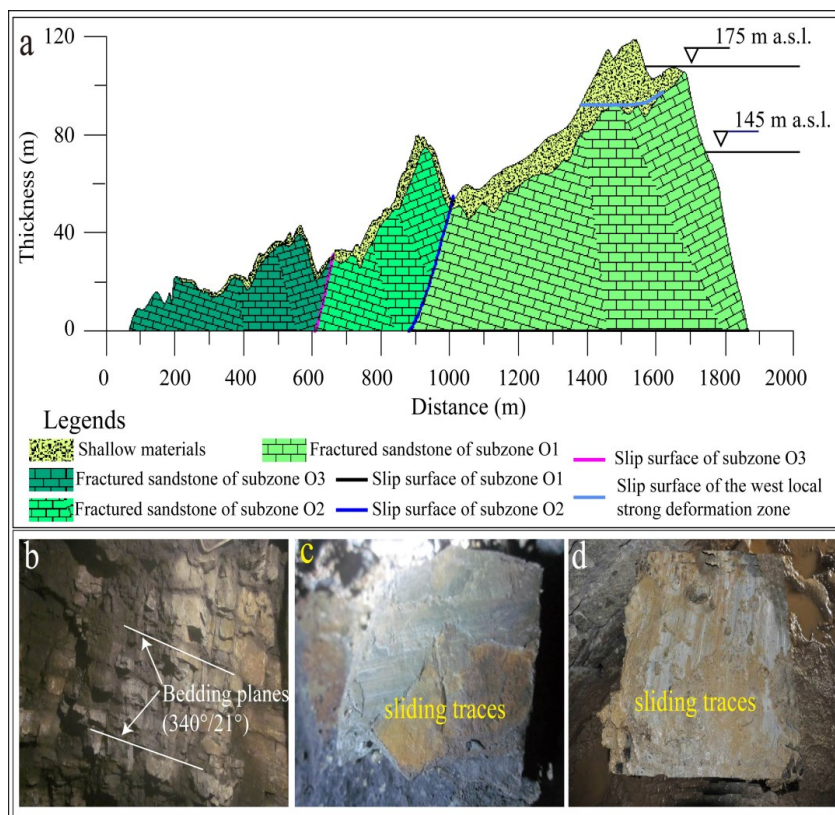


Fig. 7. Outang landslide. **a** The thickness of main body varies with the horizontal distance derived from Fig. 6a. **b** The orientation of the bedding planes within the fractured sandstone exposed by adit exploration. **c–d** Slip surfaces with clear sliding trace for two local strong deformation areas

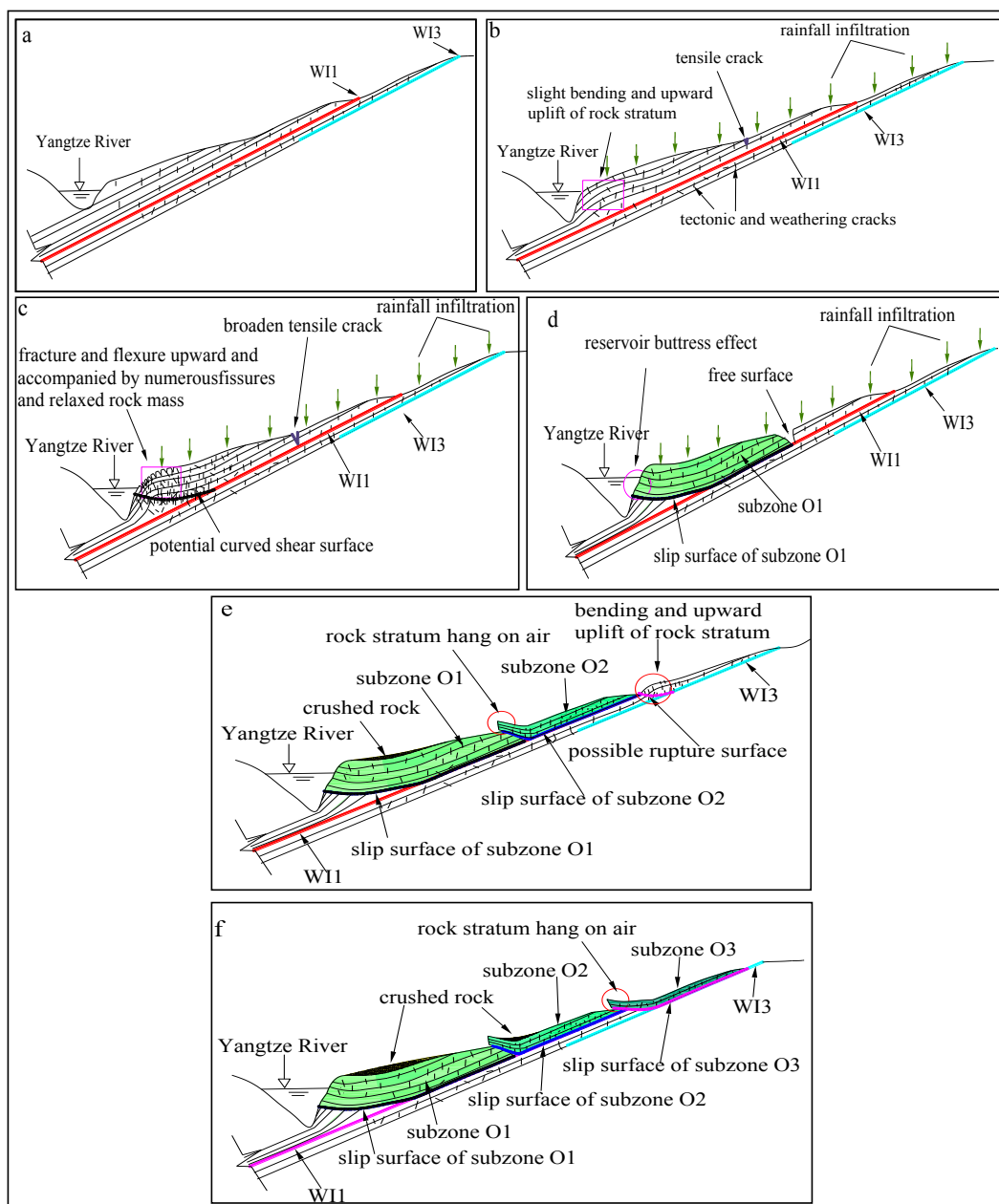


Fig. 8. The conceptual model of the formation mechanism and process for Outang landslide. **a** Fluvial incision. **b** The phenomenon of the creation of tensile crack and slight bending and upward uplift of rock stratum. **c** The fracture and flexure upward of rock mass and the occurrence of the potential curved shear surface. **d** The formation of the subzone O1 and after that the emergence of the free surface. **e** The formation of the subzone O2 and after that the possible rupture surface with bending and upward uplift of rock stratum. **f** The occurrence of the subzone O3



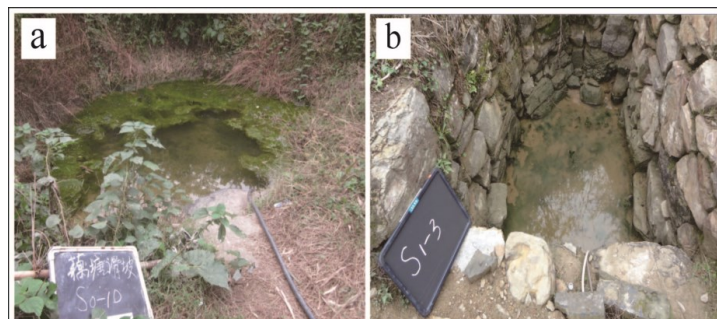


Fig. 9. Seasonal variation of groundwater exposure. **a** Spring at wet season. **b** Spring at dry season